Selective and Continuous Electrosynthesis of Hydrogen Peroxide on Nitrogen-doped Carbon Supported Nickel

Cell Reports
Physical Science

CellPress
OPEN ACCESS

Report

Selective and Continuous Electrosynthesis of Hydrogen Peroxide on Nitrogen-doped Carbon Supported Nickel

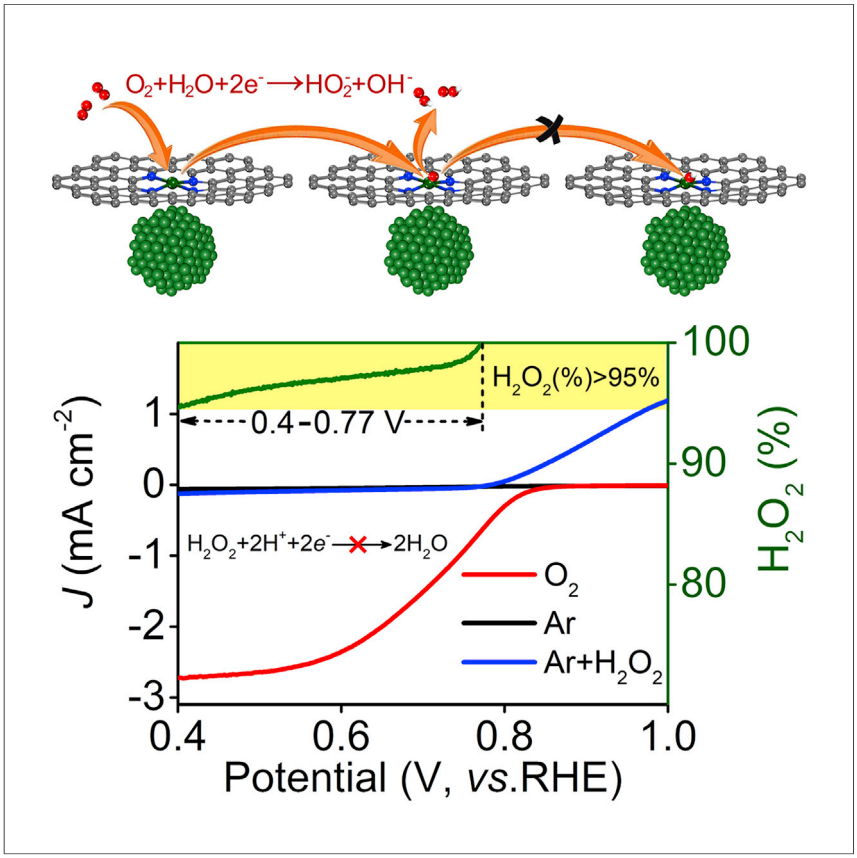

Shen et al. report that the existence of nickel particles suppresses the further reduction of hydrogen peroxide on Ni-N-C matrix, and therefore, a high selectivity >95% over a wide range of operating potentials is achieved for continuous electrosynthesis of hydrogen peroxide through two-electron oxygen electroreduction.

Hangjia Shen, Longhai Pan, Tiju Thomas, ..., Graham J. Hutchings, J. Paul Attfield, Minghui Yang

myang@nimte.ac.cn

HIGHLIGHTS

Nitrogen-doped-carbon-supported nickel is prepared for O_2 electroreduction

The optimized catalyst displays high selectivity toward H_2O_2

The nickel particles suppress the reduction of hydrogen peroxide on Ni-N-C

Shen et al., Cell Reports Physical Science 1, 100255
November 18, 2020
https://doi.org/10.1016/j.xcrp.2020.100255

Cell Reports
Physical Science

CellPress
OPEN ACCESS

Report

Selective and Continuous Electrosynthesis of Hydrogen Peroxide on Nitrogen-doped Carbon Supported Nickel

Hangjia Shen,[1,7] Longhai Pan,[1,7] Tiju Thomas,[2] Jiacheng Wang,[3] Xuyun Guo,[4] Ye Zhu,[4] Kan Luo,[1] Shiyu Du,[1] Haichuan Guo,[1] Graham J. Hutchings,[5] J. Paul Attfield,[6] and Minghui Yang[1,8,*]

SUMMARY

Hydrogen peroxide is a widely used industrial oxidant, the large-scale production of which continues to be done by an indirect process. Direct electrosynthesis of hydrogen peroxide from aerial oxygen and water is a sustainable alternative, but this remains challenging because hydrogen peroxide is highly reactive and robust catalysts are vital. Here, we report direct and continuous electrosynthesis of hydrogen peroxide under alkaline conditions using a nitrogen-doped-carbon-supported nickel catalyst. Both experiment and theoretical calculations confirm that the existence of nickel particles suppresses the further reduction of hydrogen peroxide on Ni-N-C matrix. In air-saturated 0.1 M potassium hydroxide, the energy-efficient non-precious metal electrocatalyst exhibits a consistent Faraday efficiency over 95% at a steady rate of hydrogen peroxide production (15.1 mmol min^{-1} $gcat^{-1}$) for 100 h. This sustainable, efficient, and safe process is an important step toward continuous production of hydrogen peroxide.

INTRODUCTION

Hydrogen peroxide (H_2O_2) is an environmentally friendly versatile oxidant and energy carrier with widespread relevance for chemical industries, clinical disinfection and sterilization, food manufacturing, wastewater treatment, and fuel cell operations.[1] Currently, the H_2O_2 is primarily produced through an indirect, infrastructure-heavy, and energy-intensive anthraquinone process in an organic solvent over a palladium catalyst.[2] The industrial process is capital intensive and the H_2O_2 can only be economically produced with high concentration, and this poses risks for storage and transportation. Furthermore, it does not lend itself to routine on-site application and small-scale generation of H_2O_2.[3] The direct synthesis of H_2O_2 from oxygen (O_2) is a flexible route for both large and small-scale on-site applications.[4,5] Compared to traditional oxygen hydrogenation that uses a high-pressure mixture of H_2 and O_2 at low temperatures,[6,7] electrosynthesis of H_2O_2 is promising, as this is safe and accessible even at normal pressures and temperatures.[5,8,9] The electrosynthesis route uses the cathodic oxygen reduction reaction (ORR) via a two-electron pathway to enable conversion of O_2 to H_2O_2. The fuel cell hydrogen oxidation reaction ($H_2+O_2 \rightarrow H_2O_2$) has been shown to offer continuous production,[10] but the required hydrogen is typically generated using the environmentally unfriendly water-gas shift reaction[11] or energy-intensive water electrolysis.[12]

Continuous electrosynthesis of hydrogen peroxide from water and oxygen ($1/2O_2+H_2O \rightarrow H_2O_2$) via a cathodic ORR is an ideal strategy, as the reactants are

[1]Ningbo Institute of Materials Technology and Engineering, Chinese Academy of Sciences, 1219 Zhongguan West Road, Ningbo 315201, China

[2]Department of Metallurgical and Materials Engineering, Indian Institute of Technology Madras Adyar, Chennai 600036, Tamil Nadu, India

[3]State Key Laboratory of High Performance Ceramics and Superfine Microstructure, Shanghai Institute of Ceramics, Chinese Academy of Sciences, 1295 Dingxi Road, Shanghai 200050, China

[4]Department of Applied Physics, The Hong Kong Polytechnic University, Hung Hom, Hong Kong, China

[5]Cardiff Catalysis Institute and School of Chemistry, Cardiff University, Cardiff CF10 3AT, UK

[6]Centre for Science at Extreme Conditions and School of Chemistry, University of Edinburgh, King's Buildings, Mayfield Road, Edinburgh EH9 3JZ, UK

[7]These authors contributed equally

[8]Lead Contact

*Correspondence: myang@nimte.ac.cn

https://doi.org/10.1016/j.xcrp.2020.100255

directly available, so this process is sustainable and economical. However, apart from the O_2 mass transfer at gas diffusion electrode,[13] the reaction efficiency strongly depends on the performance of the electrode materials,[9,14] which must be robust and offer high activity and selectivity over a wide range of overpotentials.[15,16] Precious-metal-free catalysts, including oxidized carbon materials,[14,17] heteroatom-doped carbon,[18,19] and metal sulfides,[20,21] have been previously reported for H_2O_2 electrosynthesis. Recently, the transition metal single-atom catalysts with metal-nitrogen-carbon configuration were widely investigated to boost ORR.[22,23] Among them, the Ni-N-C was theoretically demonstrated as highly selective site toward H_2O_2 production because of the large *OOH reduction barrier; however, the experimental value (~80%) is still unsatisfied.[24]

In this work, a noble-metal-free ORR catalyst of nitrogen-doped-carbon-supported nickel (Ni/C) is shown to have selectivity >95% over a wide range of operating potentials, enabling continuous electrosynthesis of H_2O_2 from water and air under alkaline conditions.

RESULTS AND DISCUSSION

Catalyst Preparation and Characterization

A series of Ni/C catalysts were synthesized via one-step pyrolysis at 900°C under flowing argon using Zeolitic Imidazolate Framework-8 (ZIF-8) and $Ni(NO_3)_2$ as precursors in different ratios. The elemental composition of the prepared catalyst is identified using thermogravimetry (TG) (Figure S1; Table S1). The reduced nickel is evidenced by three distinct reflections in the X-ray diffraction (XRD) patterns (Figures 1A and S2). These are assigned to the pure crystalline phase of face center cubic nickel (space group: *Fm*-3*m*) with a lattice parameter of 3.5213(3) Å. As confirmed by Ni $2p_{3/2}$ X-ray photoelectron spectroscopy (XPS) analysis (Figures 1B and S3), the majority of the surface Ni atoms in Ni/C-4 are in the metallic state (Figure 1B). It is noteworthy that no zinc is determined because the volatilization of zinc during pyrolysis. Images from transmission electron microscopy (TEM) are given in Figures 1C and S4. We observe similarities between the morphologies of samples Ni/C-2, Ni/C-3, Ni/C-4, and Ni/C-5. The notable similarity has to do with the distinct and discernible Ni nanoparticles. The selected-area electron diffraction (SAED) of a single Ni nanoparticle shows its single crystalline (Figure 1D). High-resolution TEM (HRTEM) images of Ni/C-4 on the edge of Ni nanoparticles shows well-defined fringes (Figure 1E) with a lattice spacing of 1.8 and 2.0 Å. This is consistent with what is expected of the Ni (002) and (111) plane.[25] The structure of Ni supported on nitrogen-doped carbon for Ni/C-4 is further confirmed by high-angle annular dark-field scanning TEM (HAADF-STEM) and electron energy loss spectroscopy (EELS) mapping (Figure 1F).

ORR Performance

ORR performance is evaluated on a rotating ring-disk electrode (RRDE) at 1,600 rpm (Figure S5). The disk (Figure S5A) and ring current (Figure S5B) collected over 0.40–0.77 V potential range shows that Ni/C-4 has a selectivity >95% for H_2O_2 generation (Figure 2A). The corresponding electron transfer number (n in Figure S5C) is less than 2.1. This is in agreement with the result derived from the slopes of Koutecký-Levich plots at various rotation speeds (Figure S6). The sequential reduction of H_2O_2 to H_2O (i.e., the H_2O_2 reduction reaction [HRR]) is suppressed, thereby enabling the observed target selectivity.

The reduction current at Ar-saturated solution with 3.5 mM H_2O_2 reveals that the H_2O_2 reduces to water when Ni/C-1, Ni/C-2, and Ni/C-3 are used (Figure S7). However, in the case of Ni/C-4 (Figure 2A) and Ni/C-5 (Figure S7D), the HRR current is negligible. This

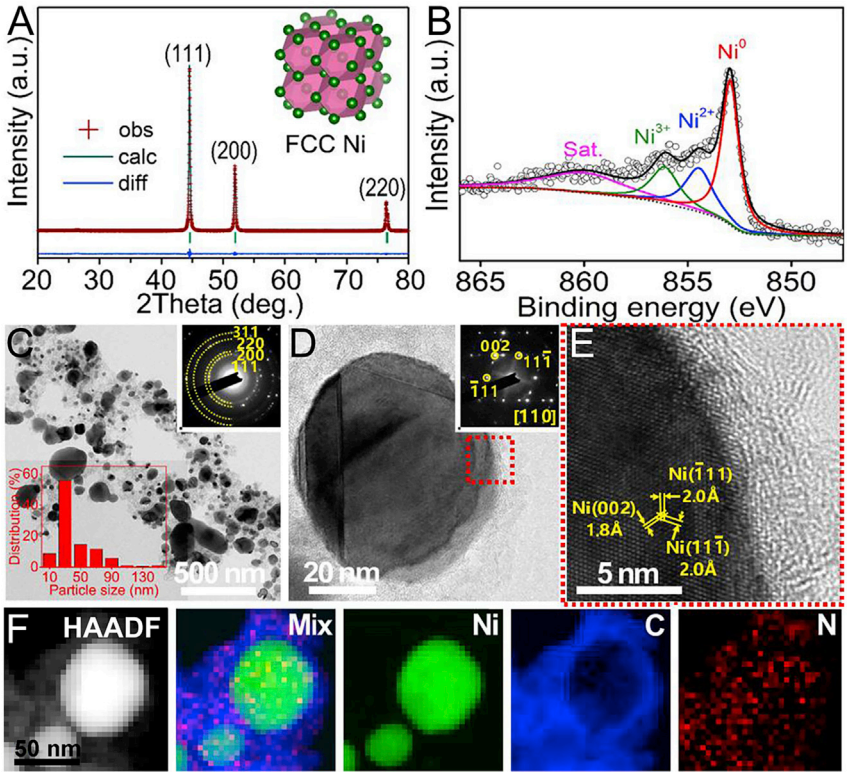

Figure 1. Structure Characterization of Ni/C-4

(A) The Rietveld fitted XRD pattern matches well with the face center cubic nickel phase (space group: *Fm*-3*m* [no. 225]; *a* = 3.5213(3) Å).

(B) XPS spectrum of the Ni2$p_{3/2}$ region.

(C) TEM image of Ni/C-4. Inset is the SAED and the Ni particle size distribution.

(D) TEM image of single Ni particle. Inset is the corresponding SAED.

(E) HR-TEM images of selected regions shown in (D). Lattice fringes of Ni with *d*-spacings of 1.8 and 2.0 Å are clearly seen.

(F) HAADF-STEM and EELS mapping images of Ni, C, and N.

indicates that the reduction of H_2O_2 is suppressed when Ni/C-4 or Ni/C-5 is used. Although metallic nickel too shows high selectivity toward H_2O_2 formation (Figure S5), its activity is significantly lower than that of the carbon-supported nickel samples.

To verify the role of the carbon, the optimum sample, i.e., Ni/C-4, is etched using HCl (2.0 M) aqueous solution. As evaluated by XRD, TG, and TEM (Figure S8), the nickel in the acid-treated sample (labeled as NFC) reduces to 0.8 wt.%. As disclosed by EELS mapping image in Figure S8C, the residual nickel is probably atomically dispersed because the pyridinic and pyrrolic nitrogen atoms can associate with Ni to form the Ni-N-C moieties.[26,27] Subsequently, from corresponding RRDE results, reduced H_2O_2 selectivity is observed when NFC is used (Figure S9). This is because the carbon atom with Lewis basicity adjacent to nitrogen[28,29] or the Ni-N-C moieties[30,31] in NFC samples favors oxygen reduction to water through a four-electron pathway. However, these active centers for the non-desired reaction are suppressed by the presence of Ni nanoparticles.

DFT Calculations

Density functional theory plus dispersion (DFT-D) calculations are performed to unravel the role that Ni nanoparticles play in the H_2O_2 electrosynthesis. According to

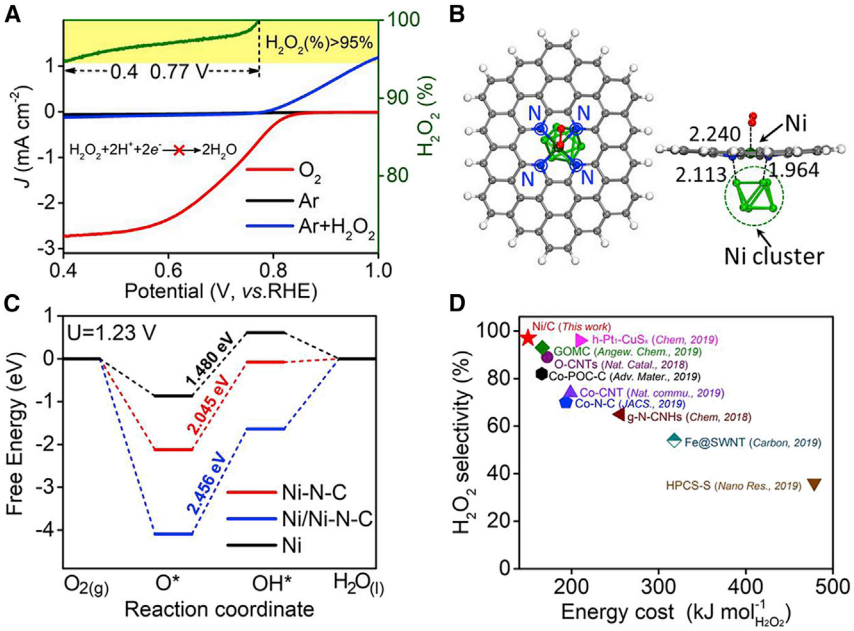

Figure 2. Electrocatalytic Performance

(A) Polarization curve of 2e$^-$ ORR. Scanning at 10 mV s^{-1} for collecting rotating ring-disk electrode voltammograms in O_2-saturated 0.1 M KOH. The reduction of H_2O_2 (HRR) is suppressed. Hence, the prepared material shows a selectivity >95% for H_2O_2 generation over a wide potential range (0.4–0.77 V).

(B) Computational model of O_2 adsorbed on Ni/C (Ni cluster modified Ni-N-C moieties).

(C) Free energy diagram for the Ni cluster, Ni-N-C, and Ni/Ni-N-C systems during the ORR at an equilibrium potential of U = 1.23 V.

(D) Comparison of Ni/C with current literature catalysts for H_2O_2 electrosynthesis.

our experimental results, three different models, namely Ni/Ni-N-C, Ni-N-C, and Ni, are constructed and shown in Figures 2B and S10. On these optimized structures, the corresponding adsorption Gibbs free energies (eV) of the reaction intermediate O* (G_{O*}), OH* (G_{OH*}) are calculated. As presented in Figure 2C and Table S2, the presence of Ni cluster improves the interaction between Ni-N-C and oxygenated species (O* and OH*). At the equilibrium potential, the reaction energy cost of reduction steps from O* to OH* on Ni/Ni-N-C is 2.045 eV, higher than that on pristine Ni-N-C (1.480 eV), indicating the higher barrier for H_2O_2 reduction on Ni/Ni-N-C, consistent with the previously reported results.[24] Therefore, the selectivity toward H_2O_2 during ORR is remarkably enhanced by the presence of Ni cluster on Ni-N-C materials. These comparative studies confirm the important role of Ni particles to improve the H_2O_2 selectivity in the prepared sample Ni/C. Thus, to achieve the optimum performance, it is ideal to keep a maximum Ni-N-C site, and all of them are adjacent to nickel particle.

These results gain importance, given that, albeit reports of use of heteroatom-doped carbon materials for electrosynthesis of H_2O_2, important challenges persist. For instance, almost uniformly, these heteroatom-doped carbons suffer from either a high overpotential or low selectivity. When the overpotential is reduced, the selectivity suffers because continuous reduction to water is not prevented in such cases. This loss in yield in turn adds to the energy cost for H_2O_2 generation (see Figure 2D and Table S3 for further details). The energy cost given in Table S3 is determined using the anodic potential value of 1.5 V for water oxidation. The energy cost for H_2O_2 production from H_2O on the prepared Ni/C catalyst is 150 kJ per mol; this

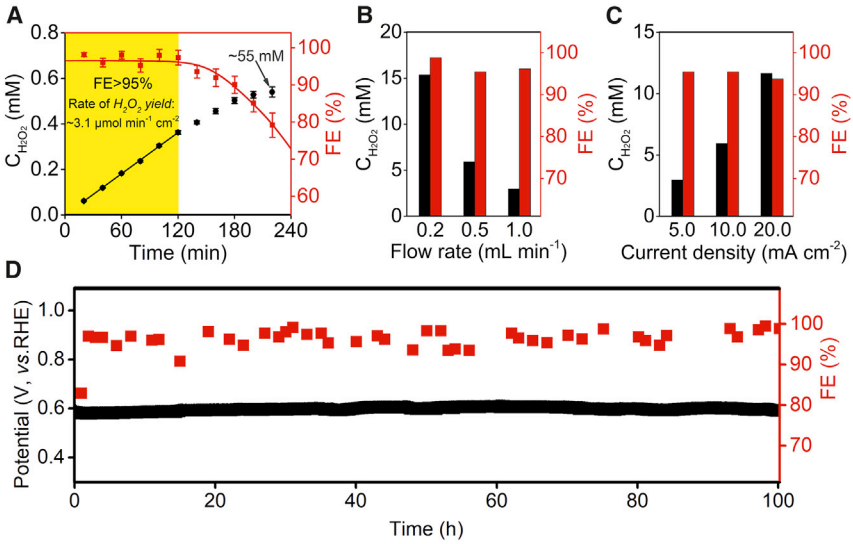

Figure 3. Electrosynthesis of H_2O_2

(A) Electrosynthesis of H_2O_2 in a fixed cell with constant volume air-saturated electrolyte at 10.0 mA cm^{-2}. A FE over 95% with a steady rate of 3.1 μmol min^{-1} cm^{-2} (i.e., 15.5 mmol min^{-1} g_{cat}^{-1}) and an equilibrium concentration of about 55 mM for H_2O_2 electrosynthesis is achieved.

(B and C) Steady-state H_2O_2 concentration and Faradaic efficiency determined using dependence on flow rate and current density in air-saturated flowing catholyte. The current density in (B) is 10.0 mA cm^{-2}, and the flow rate of catholyte in (C) is 0.2 mL min^{-1}.

(D) Stability tests for continuous generation of H_2O_2: the flow rate of catholyte is 0.2 mL min^{-1}, and the current density is kept at 10.0 mA cm^{-2}.

outperforms all the reported materials.[14,17–19,32–35] Besides, the wide potential range for highly selective electrosynthesis of H_2O_2 on Ni/C-4 offers prospects for a wide range of applications.[5]

Performance Benchmarking and Continuous H_2O_2 Production

A sensitive and efficient electroanalytical method using the oxidation of H_2O_2 ($H_2O_2 \rightarrow H_2O+1/2O_2+2e^-$) on a Pt surface has been adapted to benchmark the results reported (Figure S11).[36] The H_2O_2 yield and Faraday efficiency (FE) are measured at 10 mA cm^{-2} in a fixed electrochemical cell (Figure S12A). The potential is recorded and presented in Figure S12B. The H_2O_2 yield is analyzed via continuous sampling at 20-min intervals. H_2O_2 oxidation currents at different time intervals are detected (Figure S12C). Based on the curve obtained thus (Figure S11D), the concentration of H_2O_2 (C_{H2O2}) is calculated. As shown in Figure 3A, the electrosynthesis of H_2O_2 is conducted in a fixed cell with constant volume air-saturated electrolyte at 10.0 mA cm^{-2}. When C_{H2O2} is lower than 40 mM, we observe FE greater than 95%. This translates to a steady production rate of 3.1 μmol min^{-1} cm^{-2} (i.e., 15.5 mmol min^{-1} g_{cat}^{-1}; FE = 98%). This is higher than the previously reported value (2.5 μmol min^{-1} cm^{-2}; FE = 80%) on functionalized carbon black.[10] With increasing C_{H2O2}, the FE and the concomitant observed H_2O_2 yield decreases. This is because higher concentrations of H_2O_2 shift the equilibrium away from the $2e^-$ process and a fraction of the generated H_2O_2 decomposes.[10] An equilibrium H_2O_2 concentration of about 55 mM is finally achieved in air-saturated 0.1 M KOH.

To continuously produce H_2O_2 in air-saturated electrolyte and assess the stability of catalyst, a fixed electrochemical cell with flow electrolyte (Figure S13) has been

employed. As demonstrated in Figure 3B and 3C, the desired concentrations of H_2O_2 can be supplied via control of the experimental setup (i.e., flow rate of catholyte and current density). The Ni/C-4 reported herein shows >95% selectivity at either appropriate current density (~20 mA cm^{-2}) or fast flow rate (1.0 mL min^{-1}), higher than the state-of-the-art value (86.5%) achieved on a superhydrophobic natural air diffusion electrode.[13]

At a current density of 10 mA cm^{-2} for cathode (1.0 cm^2) and a flow rate of 0.2 mL min^{-1} of the catholyte, H_2O_2 with a constant concentration of 15.1 mM (0.051 wt.%) is continuously obtained at the output stream (Figure S14). This implies a stable rate of 3.0 μmol min^{-1} cm^{-2}. Also, the FE is consistently over 95% for 100 h (Figure 3D). No degradation of potential (Figure 3D), H_2O_2 output concentration, or FE is observed over the 100-h continuous operation. In addition, confirmed by XRD in Figure S15, the Ni/C-4 after 100 h durability measurement maintains the primary phase of face center cubic nickel. Together, these demonstrate the excellent performance of the reported material offers for selective electrochemical H_2O_2 production through $2e^-$ ORR in alkaline electrolyte.

In summary, the nitrogen-doped-carbon-supported nickel with high metal content shows excellent performance toward H_2O_2 electrosynthesis from water and air at normal pressure and temperature under alkaline conditions. The comprehensive experimental/theoretical study shows that the Ni particles improve the interaction between Ni-N-C and oxygenated species and suppress the H_2O_2 reduction during ORR. The reported efficient synthesis process in this work averts the need for use of H_2, offering an efficient, safe, and scalable process for H_2O_2 production under alkaline conditions, although electrosynthesis under neutral or acidic conditions remains an outstanding challenge.

EXPERIMENTAL PROCEDURES

Resource Availability

Lead Contact

Further information and requests for resources and reagents should be directed to and will be fulfilled by the lead contact, Minghui Yang (myang@nimte.ac.cn).

Materials Availability

This study did not generate new unique reagents.

Data and Code Availability

The data supporting the findings of this study are available from the lead contact on request.

Synthesis of the Materials

The carbon precursor ZIF-8 used in this work is synthesized according to the reported method.[37] Typically, 5.95 g $Zn(NO_3)_2 \cdot 6H_2O$ and 6.16 g 2-MeIm are dissolved in 150 mL methanol to form two clear solutions. The 2-MeIm solution is added to the $Zn(NO_3)_2$ solution, and the resulting mixed solution is stirred at room temperature for 24 h. The solid ZIF-8 product is collected using filtration and subsequently washed with methanol and dried at 60°C.

For the synthesis of carbon-doped nickel (Ni/C), 500 mg ZIF-8 is first dispersed into 75 mL ethylene glycol (EG) and then 5 mL NaOH (8.0 M) aqueous solution is added. The mixture is then stirred for 30 min. Next, pouring 20 mL EG solution with different amount of $Ni(NO_3)_2$ into the mixed solution of ZIF-8 and NaOH, stirring is continued

at 80°C for 1 h. After filtration, the product is washed using water and ethanol and vacuum dried at 60°C. The green powder obtained is finally pyrolyzed at 900°C for 2 h under flowing Ar. The final product obtained is denoted as Ni/C. The sample synthesized using 0, 0.5, 1.0, 2.0, 4.0, and 6.0 g $Ni(NO_3)_2 \cdot 6H_2O$ is designated as NC, Ni/C-1, Ni/C-2, Ni/C-3, Ni/C-4, and Ni/C-5, respectively. For comparison, a pure metallic nickel is prepared without ZIF-8 and pyrolyzed at 900°C for 2 h under flowing H_2/Ar (5% H_2). The sample Ni/C-4 is etched using hydrochloric acid (2.0 M) at 40°C for 6 h to deliver a sample NFC.

Characterization

XRD is conducted using a powder X-ray diffractometer (Rigaku Miniflex 600) with Cu-K_α radiation (λ = 1.54178 Å) in a 2θ range from 20° to 80° scanning at 1° min^{-1}. The morphology of samples is characterized using a Tecnai F20 TEM. XPS measurements are performed on a Kratos Axis Ultra DLD using 96 W Al K_α radiation. The binding energies are referenced to the C1s line at 284.8 eV from the adventitious carbon. Thermogravimetric analysis (TGA) is used to determine the Ni content of materials on a NETZSCH5 by employing a heating rate of 10°C min^{-1} from 40°C to 700°C under air. The Ni content in the sample is calculated based on the mass of final ash using the formula: Ni (wt.%) = ash (wt.%)M_{Ni}/M_{NiO}.

All electrochemical measurements are carried out on CHI 760E (Chenhua Instruments, Shanghai) without IR compensation in KOH aqueous solution (0.1 M) at room temperature (~25°C). The details are presented in Supplemental Experimental Procedures.

Theoretical Calculations

In our calculations, first-principles density functional theory plus dispersion (DFT-D) calculations are performed using the DMol3 module.[38] The generalized gradient approximation (GGA) with the Perdew and Wang (PW91) functional and Ortmann Bechstedt and Schmidt (OBS) scheme of dispersion correction is employed to describe the exchange and correlation effects.[39,40] DFT Semi-core Pseudopots (DSPP)[41] atomic orbital augmented by double numerical plus polarization (DNP+) with spin unrestricted is used as the basis set.[42] The convergence tolerances of 10^{-3} a.u./Å on the gradient, 10^{-3} Å on displacement, and 10^{-6} a.u. on the energy are adopted, respectively.

The change in Gibbs free energy ΔG for each reaction at 298.15 K with the electronic, vibrational, and entropy energy contributions included is given by the expression (Equation 1),

$$\Delta G = \Delta E + \Delta ZPE - T\Delta S + \Delta G_U + \Delta G_{pH}, \quad \text{(Equation 1)}$$

where ΔE is the reaction energy, ΔZPE is the change in zero point energy, ΔS is the change in entropy, T is temperature, $\Delta G_U = -neU$ is the effect of the electrons transfer in the electrode, and $\Delta G_{pH} = -k_B T \ln[H^+] = pH \times k_B \ln 10$ is the change of free energy owing to the pH value of the electrolyte. The Gibbs free energies for the intermediates O* and HO* are calculated by the reactions Equations 2 and 3.

$$H_2O + * \rightarrow O* + 1/2H_2 \quad \text{(Equation 2)}$$

$$H_2O + * \rightarrow HO* + H_2 \quad \text{(Equation 3)}$$

The free energy of $^1/_2O_2$ is determined by $G(^1/_2O_2) = G(H_2O) - G(H_2) + 2 \times 1.23(eV)$.

SUPPLEMENTAL INFORMATION

Supplemental Information can be found online at https://doi.org/10.1016/j.xcrp.2020.100255.

ACKNOWLEDGMENTS

This work is supported by Natural Science Foundation of China (grant no. 21471147) and National Key Research and Development Plan (grant no. 2016YFB0101205). G.J.H. thanks the CAS for financial support. H.S. would like to thank the China Postdoctoral Science Foundation (2019M652155). M.Y. would like to thank the National "Thousand Youth Talents" program of China and Ningbo 3315 program for support. J.P.A. thanks EPSRC for support. T.T. thanks the Department of Science and Technology for financial support via projects DST Solar Energy Harnessing Center and "Materials for Energy Storage."

AUTHOR CONTRIBUTIONS

M.Y., J.P.A., and G.J.H. conceived and coordinated the research. H.S., L.P., Y.Z., X.G., T.T., and H.G. synthesized and characterized the materials; K.L. and S.D. performed density functional theory calculations; and H.S., J.W., T.T., and H.G. analyzed and carried out electrochemical measurements and co-wrote the paper with G.J.H., M.Y., and J.P.A. All authors discussed the results and commented on the manuscript.

DECLARATION OF INTERESTS

The authors declare no competing interests.

Received: August 25, 2020
Revised: September 27, 2020
Accepted: October 21, 2020
Published: November 18, 2020

REFERENCES

1. Eul, W., Moeller, A., and Steiner, N. (2000). Hydrogen peroxide. Kirk-Othmer Encyclopedia of Chemical Technology (John Wiley and Sons).

2. Lee, N.D. (1971). Production of hydrogen peroxide by anthraquinone process. US patent US3615207A, filed June 16, 1969, and granted October 26, 1971.

3. Kosydar, R., Drelinkiewicz, A., and Ganhy, J.P. (2010). Degradation reactions in anthraquinone process of hydrogen peroxide synthesis. Catal. Lett. *139*, 105–113.

4. Campos-Martin, J.M., Blanco-Brieva, G., and Fierro, J.L.G. (2006). Hydrogen peroxide synthesis: an outlook beyond the anthraquinone process. Angew. Chem. Int. Ed. Engl. *45*, 6962–6984.

5. Perry, S.C., Pangotra, D., Vieira, L., Csepei, L.-I., Sieber, V., Wang, L., Ponce de León, C., and Walsh, F.C. (2019). Electrochemical synthesis of hydrogen peroxide from water and oxygen. Nat. Rev. Chem. *3*, 442–458.

6. Edwards, J.K., Solsona, B., N, E.N., Carley, A.F., Herzing, A.A., Kiely, C.J., and Hutchings, G.J. (2009). Switching off hydrogen peroxide hydrogenation in the direct synthesis process. Science *323*, 1037–1041.

7. Freakley, S.J., He, Q., Harrhy, J.H., Lu, L., Crole, D.A., Morgan, D.J., Ntainjua, E.N., Edwards, J.K., Carley, A.F., Borisevich, A.Y., et al. (2016). Palladium-tin catalysts for the direct synthesis of H_2O_2 with high selectivity. Science *351*, 965–968.

8. Yang, S., Verdaguer-Casadevall, A., Arnarson, L., Silvioli, L., Čolić, V., Frydendal, R., Rossmeisl, J., Chorkendorff, I., and Stephens, I.E.L. (2018). Toward the decentralized electrochemical production of H_2O_2: a focus on the catalysis. ACS Catal. *8*, 4064–4081.

9. Jiang, Y., Ni, P., Chen, C., Lu, Y., Yang, P., Kong, B., Fisher, A., and Wang, X. (2018). Selective electrochemical H_2O_2 production through two-electron oxygen electrochemistry. Adv. Energy Mater. *8*, 1801909.

10. Xia, C., Xia, Y., Zhu, P., Fan, L., and Wang, H. (2019). Direct electrosynthesis of pure aqueous H_2O_2 solutions up to 20% by weight using a solid electrolyte. Science *366*, 226–231.

11. Pal, D.B., Chand, R., Upadhyay, S.N., and Mishra, P.K. (2018). Performance of water gas shift reaction catalysts: a review. Renew. Sustain. Energy Rev. *93*, 549–565.

12. Dincer, I., and Acar, C. (2015). Review and evaluation of hydrogen production methods for better sustainability. Int. J. Hydrogen Energy *40*, 11094–11111.

13. Zhang, Q., Zhou, M., Ren, G., Li, Y., Li, Y., and Du, X. (2020). Highly efficient electrosynthesis of hydrogen peroxide on a superhydrophobic three-phase interface by natural air diffusion. Nat. Commun. *11*, 1731.

14. Lu, Z., Chen, G., Siahrostami, S., Chen, Z., Liu, K., Xie, J., Liao, L., Wu, T., Lin, D., Liu, Y., et al. (2018). High-efficiency oxygen reduction to hydrogen peroxide catalysed by oxidized carbon materials. Nat. Catal. *1*, 156–162.

15. Couper, A.M., Pletcher, D., and Walsh, F.C. (1990). Electrode materials for electrosynthesis. Chem. Rev. *90*, 837–865.

16. Siahrostami, S., Verdaguer-Casadevall, A., Karamad, M., Deiana, D., Malacrida, P., Wickman, B., Escudero-Escribano, M., Paoli, E.A., Frydendal, R., Hansen, T.W., et al. (2013). Enabling direct H_2O_2 production through rational electrocatalyst design. Nat. Mater. *12*, 1137–1143.

17. Sa, Y.J., Kim, J.H., and Joo, S.H. (2019). Active edge-site-rich carbon nanocatalysts with enhanced electron transfer for efficient electrochemical hydrogen peroxide production. Angew. Chem. Int. Ed. Engl. *58*, 1100–1105.

18. Chen, G., Liu, J., Li, Q., Guan, P., Yu, X., Xing, L., Zhang, J., and Che, R. (2019). A direct H_2O_2 production based on hollow porous carbon sphere-sulfur nanocrystal composites by confinement effect as oxygen reduction electrocatalysts. Nano Res. *12*, 2614–2622.

19. Iglesias, D., Giuliani, A., Melchionna, M., Marchesan, S., Criado, A., Nasi, L., Bevilacqua, M., Tavagnacco, C., Vizza, F., Prato, M., and Fornasiero, P. (2018). N-doped graphitized carbon nanohorns as a forefront electrocatalyst in highly selective O_2 reduction to H_2O_2. Chem *4*, 106–123.

20. Xing, M., Xu, W., Dong, C., Bai, Y., Zeng, J., Zhou, Y., Zhang, J., and Yin, Y. (2018). Metal sulfides as excellent co-catalysts for H_2O_2 decomposition in advanced oxidation processes. Chem *4*, 1359–1372.

21. Sheng, H., Hermes, E.D., Yang, X., Ying, D., Janes, A.N., Li, W., Schmidt, J.R., and Jin, S. (2019). Electrocatalytic production of H_2O_2 by selective oxygen reduction using Earth-abundant cobalt pyrite (CoS_2). ACS Catal. *9*, 8433–8442.

22. He, Y., Tan, Q., Lu, L., Sokolowski, J., and Wu, G. (2019). Metal-nitrogen-carbon catalysts for oxygen reduction in PEM fuel cells: self-template synthesis approach to enhancing catalytic activity and stability. Electrochem. Energy Rev. *2*, 231–251.

23. Yin, H., Dou, Y., Chen, S., Zhu, Z., Liu, P., and Zhao, H. (2020). 2D electrocatalysts for converting Earth-abundant simple molecules into value-added commodity chemicals: recent progress and perspectives. Adv. Mater. *32*, e1904870.

24. Gao, J., Yang, H., Huang, X., Hung, S.-F., Cai, W., Jia, C., Miao, S., Chen, H.M., Yang, X., Huang, Y., et al. (2020). Enabling direct H_2O_2 production in acidic media through rational design of transition metal single atom catalyst. Chem *6*, 658–674.

25. Hu, X., and Yu, J.C. (2008). High-yield synthesis of nickel and nickel phosphide nanowires via microwave-assisted processes. Chem. Mater. *20*, 6743–6749.

26. Qu, Y., Li, Z., Chen, W., Lin, Y., Yuan, T., Yang, Z., Zhao, C., Wang, J., Zhao, C., Wang, X., et al. (2018). Direct transformation of bulk copper into copper single sites via emitting and trapping of atoms. Nat. Catal. *1*, 781–786.

27. Ju, W., Bagger, A., Hao, G.-P., Varela, A.S., Sinev, I., Bon, V., Roldan Cuenya, B., Kaskel, S., Rossmeisl, J., and Strasser, P. (2017). Understanding activity and selectivity of metal-nitrogen-doped carbon catalysts for electrochemical reduction of CO_2. Nat. Commun. *8*, 944.

28. Gong, K., Du, F., Xia, Z., Durstock, M., and Dai, L. (2009). Nitrogen-doped carbon nanotube arrays with high electrocatalytic activity for oxygen reduction. Science *323*, 760–764.

29. Guo, D., Shibuya, R., Akiba, C., Saji, S., Kondo, T., and Nakamura, J. (2016). Active sites of nitrogen-doped carbon materials for oxygen reduction reaction clarified using model catalysts. Science *351*, 361–365.

30. Peng, H., Liu, F., Liu, X., Liao, S., You, C., Tian, X., Nan, H., Luo, F., Song, H., Fu, Z., and Huang, P. (2014). Effect of transition metals on the structure and performance of the doped carbon catalysts derived from polyaniline and melamine for ORR application. ACS Catal. *4*, 3797–3805.

31. Mao, J., Liu, P., Li, J., Liang, D., Yan, J., and Song, W. (2019). Proliferating oxygen reduction reaction by high volume of mesopores in regular nickel–nitrogen codoped carbon nanocubes. Adv. Mater. Interfaces *6*, 1901186.

32. Li, B.-Q., Zhao, C.-X., Liu, J.-N., and Zhang, Q. (2019). Electrosynthesis of hydrogen peroxide synergistically catalyzed by atomic $Co–N_x–C$ sites and oxygen functional groups in noble-metal-free electrocatalysts. Adv. Mater. *31*, 1808173.

33. Sun, Y., Silvioli, L., Sahraie, N.R., Ju, W., Li, J., Zitolo, A., Li, S., Bagger, A., Arnarson, L., Wang, X., et al. (2019). Activity-selectivity trends in the electrochemical production of hydrogen peroxide over single-site metal-nitrogen-carbon catalysts. J. Am. Chem. Soc. *141*, 12372–12381.

34. Jiang, K., Back, S., Akey, A.J., Xia, C., Hu, Y., Liang, W., Schaak, D., Stavitski, E., Nørskov, J.K., Siahrostami, S., and Wang, H. (2019). Highly selective oxygen reduction to hydrogen peroxide on transition metal single atom coordination. Nat. Commun. *10*, 3997.

35. Shen, R., Chen, W., Peng, Q., Lu, S., Zheng, L., Cao, X., Wang, Y., Zhu, W., Zhang, J., Zhuang, Z., et al. (2019). High-concentration single atomic Pt sites on hollow CuS_x for selective O_2 reduction to H_2O_2 in acid solution. Chem *5*, 2099–2110.

36. Karam, P., and Halaoui, L.I. (2008). Sensing of H_2O_2 at low surface density assemblies of Pt nanoparticles in polyelectrolyte. Anal. Chem. *80*, 5441–5448.

37. Pan, Y., Sun, K., Liu, S., Cao, X., Wu, K., Cheong, W.-C., Chen, Z., Wang, Y., Li, Y., Liu, Y., et al. (2018). Core-shell ZIF-8@ZIF-67-derived CoP nanoparticle-embedded N-doped carbon nanotube hollow polyhedron for efficient overall water splitting. J. Am. Chem. Soc. *140*, 2610–2618.

38. Delley, B. (2000). From molecules to solids with the $DMol^3$ approach. J. Chem. Phys. *113*, 7756.

39. Perdew, J.P., and Wang, Y. (1992). Accurate and simple analytic representation of the electron-gas correlation energy. Phys. Rev. B Condens. Matter *45*, 13244–13249.

40. Ortmann, F., Bechstedt, F., and Schmidt, W.G. (2006). Semiempirical van der Waals correction to the density functional description of solids and molecular structures. Phys. Rev. B *73*, 205101.

41. Delley, B. (2002). Hardness conserving semilocal pseudopotentials. Phys. Rev. B *66*, 155125.

42. Delley, B. (2006). Ground-state enthalpies: evaluation of electronic structure approaches with emphasis on the density functional method. J. Phys. Chem. A *110*, 13632–13639.